eprints@whiterose.ac.uk
https://eprints.whiterose.ac.uk/

Design and testing of a frictionless mechanical inerter device using living-hinges

E. D. A. John and D. J. Wagg

Department of Mechanical Engineering, University of Sheffield, S1 3JD, UK

Abstract

In this paper a novel type of frictionless mechanical inerter device is presented, where instead of gears, motion of the flywheel is achieved using *living-hinges*. The design is a type of *pivoted flywheel inerter* inspired in part by the Dynamic Anti-resonant Vibration Isolator (DAVI) concept, which was first developed in the 1960s. Unlike the DAVI, it will be shown that the pivoted flywheel inerter has the advantage of producing balanced forces. Furthermore the use of living-hinges eliminates the need for gears or other frictional elements in the inerter mechanism. To demonstrate the utility of the new concept, a bench-top experiment was performed using a small-scale living-hinge inerter manufactured using polypropylene hinges. By estimating the experimental system parameters, the transmissibility results from the experiment could be compared to a mathematical model. These results showed that the living-hinge inerter provided an isolation effect of at least three orders of magnitude in terms of the maximum amplitude reduction from the uncontrolled system compared to that with the inerter added. Although friction was eliminated, the living-hinges did introduce additional damping, and this was found to correspond to an increase in the equivalent damping ratio for the uncontrolled system of 1.2%. It is shown that the living-hinge inerter developed in this paper fits all of the essential conditions required to be a practical inerter device. Furthermore, as it operates without mechanical friction, or fluid flow, it represents a new paradigm in experimental inerter technology.

Keywords:
Inerter, Living-hinge, Flywheel, Experiment, DAVI, Isolator

1. Introduction

Inerters have received a large amount of attention in recent literature following the work of [1]. The primary interest has been to develop inerters for use in passive vibration control devices in combination with other mechanical components such as springs, and viscous dampers. Until now, the physical realisation of inerters has been either as a mechanical device with some form of gearing, or as a fluid based device. All such designs have significant amounts of inherent damping, either from friction between mechanical components, such as gears, or from the fluid flow inside the device. This can limit the effectiveness of the inerter in many applications. As a result, it is of significant interest to create new designs that reduce these inherent damping effects. In this paper a novel type of frictionless mechanical inerter device is presented, where the gearing is eliminated, and motion is achieved using *living-hinges*.

The new inerter device is related to much older designs, before the term inerter was even defined. Specifically, this new design is partly inspired by the Dynamic Anti-resonant Vibration Isolator (DAVI) concept [2], first patented in 1967. The anti-resonance in the DAVI was exploited in the aerospace industry for applications including isolating the fuselage of a helicopter against the vibration caused by its rotors [3]. A more recent application of the DAVI was minimising vibration transmission in underwater vehicles [4]. DAVIs work on exactly the same principle as an inerter, and can be shown to have an inertance in the same way as other mechanical inerters, typically restricted to small displacement amplitudes — see for example the detailed mathematical analysis given in [5, 6].

Beyond its direct application, the DAVI concept was also used to schematically represent the inertial effect of the first fluid inerter design. This fluid inerter was incorporated into automotive engine mounts [7], where the DAVI lever arm model was used to approximate the effect of a rotating annulus of fluid (called the *inertia track*) inside the mount — see also [8–10]. In addition to this, applications of inerter-like devices in civil engineering evolved from modifications to viscous dampers, that date back to the late 1990s, and eventually resulted in tuned-viscous-mass-dampers — see the discussion in [11] and references therein.

Since the introduction of the inerter concept, it has been developed for use in many more applications. One of the first of these was in Formula 1 racing car suspension systems, under the name of the J-damper [12]. A wide range of other applications have been undertaken, including vehicle suspensions & steering systems [13–18], train suspension systems [19, 20], and civil engineering systems — see for example [21–27] and references therein.

2

Flywheel inerter devices have been considered by a number of authors, including those with a mechanical flywheel [14, 28, 29] and devices using a *fluid flywheel* effect [30–32]. Inerter devices are also referred to in some literature as *gyro-mass* devices, see for example the discussion in [33] and references therein.

This paper is structured as follows. In Section 2 the design of the new inerter is described, including a method for estimating the inertance values of the new device. Then in Section 3 the experimental testing procedure is presented in detail. A comparison between the experimental results and numerically simulated results are presented in Section 4. Finally conclusions are drawn in Section 5.

2. Design of the inerter device

The concept of an ideal inerter and inertance as a system property was introduced by Smith in 2002 [1], who also defined a set of conditions which an inerter must meet in order to be of practical use. These are:

1. The device should be capable of having a small mass, independent of the required value of inertance
2. There should be no need to attach any point of the physical device to the mechanical ground
3. The device should have a finite linear travel which is specifiable, and the device should be subject to reasonable constraints on its overall dimensions
4. The device should function adequately in any spatial orientation and motion

It will be demonstrated that the living-hinge inerter described in this paper satisfies all these conditions. The DAVI concept, patented by [2], can also be specified such that it satisfies the above design conditions. The DAVI uses the inertia of a mass attached to a lever to generate an anti-resonance, where the two terminals of the device are the fulcrums (or pivot points) attached to the lever. This is shown schematically in Figure 1 (a). In Figure 1 (b) we show the design used in this paper, where instead of a lever arm and mass, a rotating flywheel is used, and the lever arm effect is achieved by having two connection points, one offset and one at the centre of the flywheel. This idea is independent of the living-hinges, and can be implemented using pivoted attachment points as an alternative to living-hinges to give a *pivoted flywheel inerter*.

However, to eliminate friction effects entirely from the design, living-hinges were selected to provide the pivoting effect. It should be noted, that although living-hinges eliminate friction, there is still some energy loss, during the flexing process, which will be discussed further in Section 2.2. Next we consider

the mathematical model of the pivoted flywheel inerter, before proceeding to a detailed design of the pivoting mechanism provided by living-hinges.

2.1. Mathematical model for the pivoted flywheel inerter

A mathematical model for the DAVI system was first developed by [2], using the assumptions of linearity and small deflections. Even so, because of the asymmetric nature of the system (see Figure 1 (a)), the equation of motion includes both a pure inertance term and a second inertial term related to the geometry of the lever arm [5].

The pivoted flywheel design effectively eliminates this asymmetry, and as a result the physics can be captured by just a pure inertance term. We note that to fully eliminate the asymmetry, the pivots would need to be equally spaced from the centre, however the design with one pivot offset and one close to the centre was easier to implement from a practical perspective. Assuming the asymmetry has been removed, the flywheel produces a couple equal to $F\ell_a$, where F is the force on each of the pivots. The couple can be directly related to the torque, T, and the angular acceleration via

$$T = F\ell_a = I\ddot{\theta} \tag{1}$$

where I is the moment of inertia of the flywheel, θ is the angle of rotation and an overdot represents differentiation with respect to time, t. Using trigonometry we can define

$$\sin(\theta) = \frac{y - x}{\ell_a} \approx \theta \quad \rightsquigarrow \quad \ddot{\theta} = \frac{\ddot{y} - \ddot{x}}{\ell_a} \tag{2}$$

for small values of θ, meaning small displacements. The justification for this approximation is that the small angle approximation results in less than 5% error for angular displacements of less than $10.4°$. As a result we applied the constraint that

$$\frac{y - x}{\ell_a} < 0.18, \tag{3}$$

in order to reduce errors to 5% or less.

Now the pivot force can be expressed as

$$F = b(\ddot{y} - \ddot{x}), \tag{4}$$

where the inertance, b, is defined as

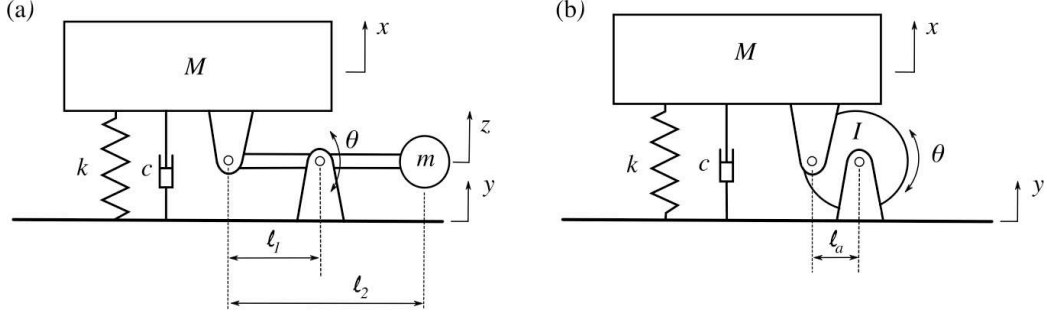$$b = \frac{I}{\ell_a^2}. \tag{5}$$

4

Figure 1: (a) Schematic diagram of the DAVI system patented by [2], and (b) the pivoted flywheel inerter considered in this paper.

Now the equation of motion for the pivoted flywheel inerter system is

$$M\ddot{x} + k(x - y) + c(\dot{x} - \dot{y}) + b(\ddot{x} - \ddot{y}) = 0, \tag{6}$$

where c is a nominal viscous damping parameter that represents the sum of all physical damping processes in the new device. Equation 6 is exactly the same as the inerter isolator system defined previously by others — see for example the derivation in [34], and other references therein.

Equation (6) leads to an *undamped* ($c = 0$) transmissibility relationship of

$$\frac{X}{Y} = \frac{k - b\omega^2}{k - (M + b)\omega^2} \tag{7}$$

where X and Y are the displacement amplitudes of x and y respectively, and ω is the frequency of the sinusoidal support motion. For this undamped system, there are two important frequency values

$$\omega_a = \sqrt{\frac{k}{b}} \quad \text{and} \quad \omega_r = \sqrt{\frac{k}{M + b}} \tag{8}$$

where ω_a is the frequency where the anti-resonance occurs (the zero of (7)), and ω_r is the resonance frequency of the isolated system (the pole of (7)).

The damped transmissibility function becomes

$$\frac{X}{Y} = \frac{k - b\omega^2 + ic\omega}{k - (M + b)\omega^2 + ic\omega} \quad \rightsquigarrow \quad \left|\frac{X}{Y}\right| = \sqrt{\frac{(1 - \mu\hat{\omega}^2)^2 + (2\zeta\hat{\omega})^2}{(1 - (1 + \mu)\hat{\omega}^2)^2 + (2\zeta\hat{\omega})^2}} \tag{9}$$

where c is the viscous damping coefficient, $\mu = b/M$ is the inertance to mass ratio, $\hat{\omega} = \omega/\omega_n$ is the frequency ratio, $\zeta = c/2M\omega_n$ is the damping ratio, and
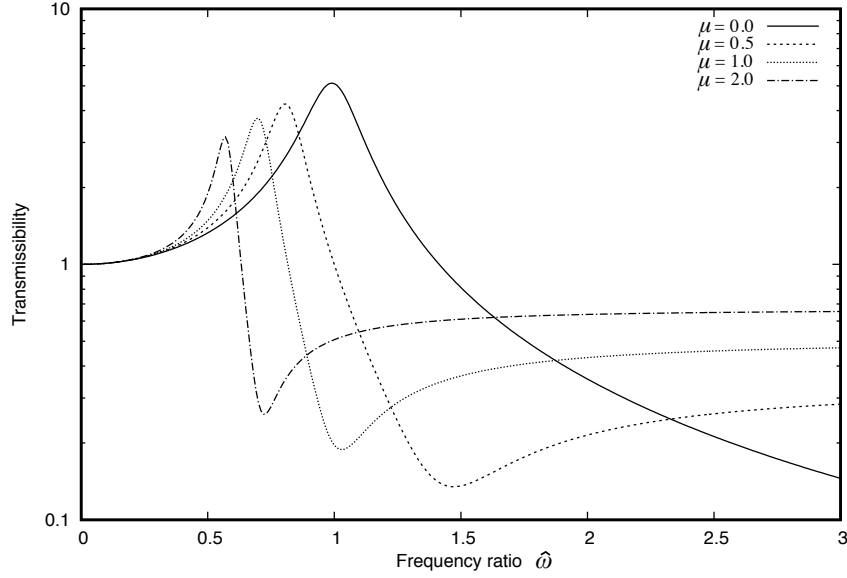
Figure 2: Support excited transmissibility numerically calculated from Equation (9) for a range of inertance to mass ratios and plotted in terms of transmissibility against frequency ration $\hat{\omega}$. For each value of μ, damping ratio $\zeta = 0.1$. Similar plots have been presented by others previously, see for example [34].

$\omega_n = \sqrt{k/M}$ is the undamped natural frequency of the uncontrolled system (if the inerter is removed i.e. $b = 0$). We note also that due to the standard assumption used in the transmissibility derivation, that $\ddot{x} = -\omega^2 x$ and $\ddot{y} = -\omega^2 y$, we can obtain the following relation

$$\frac{\ddot{x}}{\ddot{y}} = \frac{X}{Y} \rightsquigarrow \left|\frac{\ddot{x}}{\ddot{y}}\right| = \left|\frac{X}{Y}\right| \tag{10}$$

which will be used when comparing this model to experimentally recorded acceleration signals in Section 4.

Using Equation (9), Figure 2 illustrates how the transmissibility of a support excited system varies as the inertance of the system is increased with respect to the system's mass. It can clearly be seen that increasing the inertance reduces the system's natural frequency and introduces an anti-resonance [35].

To be specific about the range over which these equations of motion are valid, we selected a 80 mm diameter flywheel for the test model (and other dimensions were selected accordingly, see Appendix A for details). Time-domain numerical simulations were used to compute the forces produced for this size flywheel. It
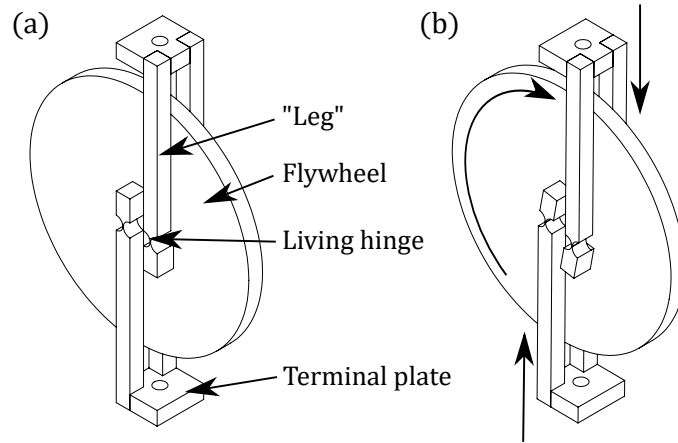
6

Figure 3: (a) Living-hinge inerter design developed from the pivoted flywheel inerter concept. Terminal plates were tapped for M5 bolts. (b) Relative displacement of the terminal plates causes rotation of the flywheel. Note deflection of the living-hinges.

was found that the small angle approximation results in less than 5% peak force error for angular displacements of less than $10.4°$ which is in accordance with the approximation given in (3).

2.2. Living-hinge design

Living-hinges (also sometimes known as integral hinges) are typically associated with plastic design and may be defined as thin, flexible webs that connect two relatively rigid adjacent sections. The living-hinge inerter used here was achieved by replacing the pivots in the pivoted flywheel inerter with notch type, semi-circular living-hinges, as discussed above, and shown in Figure 1. The living-hinge inerter design is shown schematically in Figure 3, where the addition of vertical *legs* are shown to transmit forces from the hinges (i.e. the effective pivot points) to the exterior connection points of the device.

A notch type living-hinge was selected as the preferred type for this application, as this permits greater control over the location of the hinge rotational axis, compared to longer strap hinges [36]. The fact that this is at the expense of smaller allowable deflection angles was not an issue due to the angular deflection limits already discussed. The most commonly used material for living-hinges is polypropylene as it is able to flex millions of times before failing, whereas other plastics can only flex a few thousand times before failure [37, 38]. Metallic living-hinges are also possible, however these were not considered in this current study.

7

From [36], the maximum thickness, $\hat{t}$(m), of a notch hinge for a given maximum deflection, θ_{max}(radian), to avoid plastic yielding can be determined from

$$\hat{t} = \left(\frac{\varepsilon_y}{\theta_{max}}\right)^2 \frac{9\pi^2 r}{16K^2}. \tag{11}$$

where, K, is the stress concentration factor is given by

$$K = (1 + \beta)^{\frac{9}{20}} \tag{12}$$

and β is a function of hinge thickness, $\hat{t}$, and notch radius, r

$$\beta = \frac{\hat{t}}{2r} \tag{13}$$

σ_y(N/m^2) is yield stress, and E(N/m^2) is Young's modulus.

Equations (11) and (12) can now be rearranged to give a description of θ_{max} in terms of yield strain, ε_y, and the geometry of the hinge as

$$\theta_{max} = \sqrt{\frac{9\pi^2}{32\beta(1+\beta)^{\frac{9}{10}}}} \varepsilon_y. \tag{14}$$

Values of Yield Stress and Young's Modulus for the polypropylene were 35.4 MPa and 1.6 GPa, respectively, giving Yield Strain as 0.0221. Equation (14) was solved for β numerically, and the results for a range of β values is shown in Figure 4. Using this method, the β value for a $\theta_{max}/\varepsilon_y$ of 471 (where $\theta_{max} = 10.4°$), was found to be $\beta = 0.03979$. The required hinge thickness was then found using the identity

$$\hat{t}_{max} = \frac{w\beta}{\beta + 1} \tag{15}$$

where w is the width of the material the hinge is built into i.e. $w = 2r + \hat{t}$. For a leg width of 5 mm, the hinge thickness was calculated as 0.191 mm.

Living-hinges typically have thicknesses of 0.3 - 0.5 mm ([37] pp 219–260) and at the upper range, for larger angular displacements plastic deformation would occur. The thickness of 0.191mm calculated here is slightly smaller than this, and combined with small displacements we expect elastic deformation only to occur. As a result, this value was considered acceptable for use in the living-hinge inerter test model constructed here.
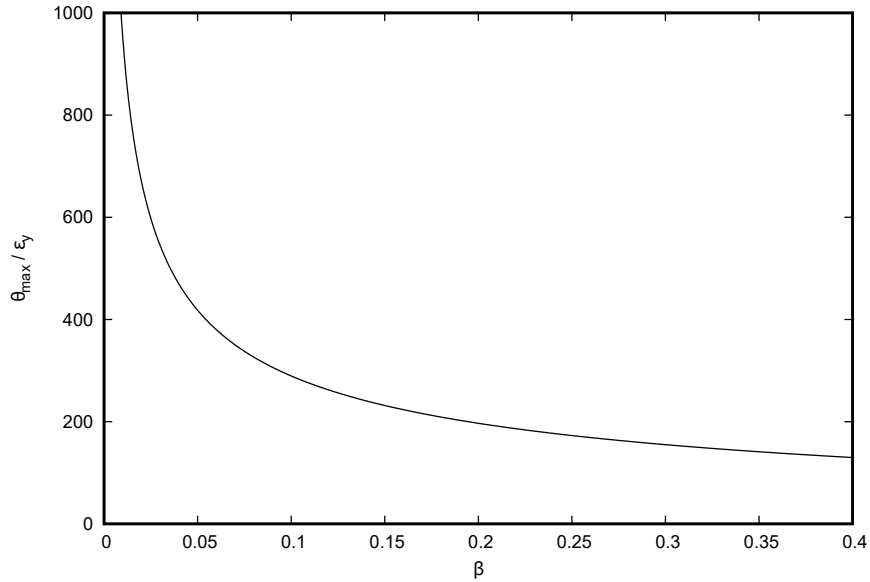
Figure 4: Plot of $\theta_{max}/\varepsilon_y$ against β calculated using Equation (14).

2.3. *Final design*

Additional changes made to the final design were the inclusion of an additional pair of legs to improve the stability of the model and 5 mm thick plates at each terminal for fitting the inerter to the test rig. As well as improving stability, the extra pair of legs reduced the stresses that each hinge was required to transmit. The final living-hinge inerter design is shown in Figure 3.

The legs were machined from polypropylene (including the hinges) and the flywheel and terminal plates were laser cut from perspex. Given the measured flywheel mass of 0.0268 kg, the inerter test model was predicted using Equation (3) to have an inertance of 0.214 kg. The measured mass of the entire living-hinge inerter test model was 0.036 kg. These values give a predicted inertance to mass ratio of 5.94. This is significantly less than the inertance to mass ratios of many previous experimental inerters. For example an inertance to mass ratio of greater than 300 is quoted in [1] for a ball-screw mechanical inerter.

As our inerter design is radically different from any previous designs, it should not be surprising that the inertance to mass ratios are quite different. In particular, we have used very low density, lightweight materials, and small-scale test rigs, with low amplitude vibrations, all of which will naturally lead to low levels of mass and inertance. However, as with all mechanical inerter designs, increasing

9

the inertance to mass ratio can be achieved by increasing the gearing of the device. To increase the gearing of the inerter design presented here the lever arm length, ℓ_a, must be decreased. This is possible in principle. for example, halving ℓ_a to 5 mm would increase the inertance to mass ratio to 23.8. However, as the aim of this paper is to introduce and demonstrate the feasibility of the living-hinge inerter, using just a single inertance to mass ratio of 5.94 was considered to be justified.

3. Experimental procedure

The majority of inerter tests in the literature to-date have been performed by fixing one terminal of the inerter and applying a displacement to the other. This type of test permits tight control over the relative terminal displacement of the inerter but does not exploit the two terminal nature of the inerter, or demonstrate its vibration isolation abilities. For this reason, a support-excited two-terminal test was used in this study. A support excited oscillator system with sprung mass $m =$ 0.46 kg and spring stiffness $k =$ 15.9 kN/m was constructed, with an electromagnetic shaker to provide a sinusoidal input to the support attachment point.

A photograph of the experimental test rig is shown in Figure 5, from which it can be seen that the shaker and inerter test system are suspended from a cantilever support that is clamped securely to a test bench. The advantage of suspending the inerter system is that there is no requirement for bearings or supports that might add unwanted friction damping to the device. The potential disadvantage is that unwanted lateral vibrations can occur, and all tests were monitored carefully to ensure this type of motion did not have a significant effect on the results. Furthermore, although the dominant motion was in the vertical direction, the motion of the mass in other directions was sensitive to the overall mass distribution of the test specimen and inerter. As a result careful attention was paid to this aspect, to ensure that the dominant displacements remained in the vertical direction, and that any sway motions were minimised to the point of being insignificant.

Data was gathered from the inerter test system using accelerometers at each terminal of the springs/inerter, and a close up photograph showing these sensors can be seen in Figure 7 (b). All accelerometers used in this study were of the type PCB Piezotronics model 353B18. This photograph also shows the living-hinge inerter system in the centre, between the three springs that are positioned in a triangular arrangement around the inerter. Furthermore, it can be seen that the flywheel has four black lines marking it into quadrants. This was to assist
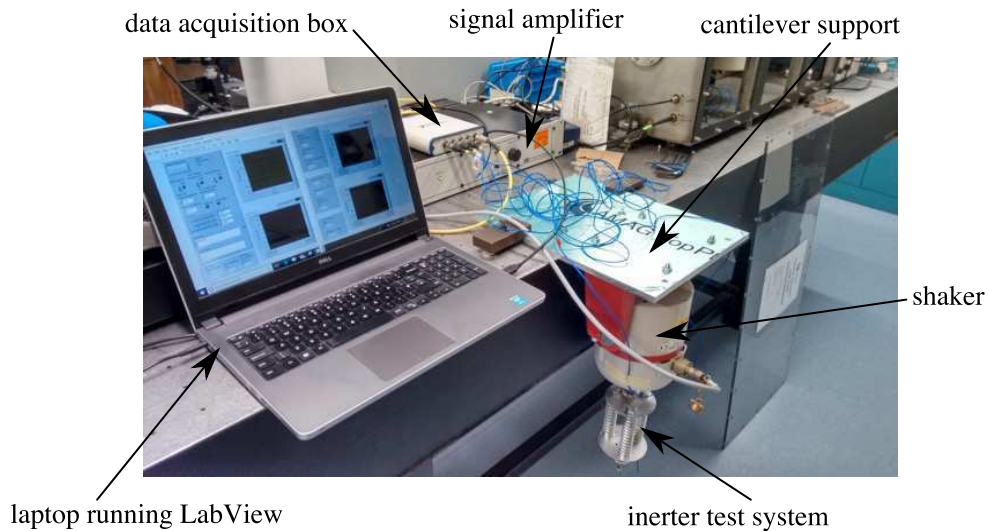
Figure 5: Photograph of the experimental set-up in the University of Sheffield Jonas Laboratory.

visualisation of the inerter motion, and the interested reader can find videos of the inerter system in the supplemental material supplied with this paper.

Also shown in Figure 5 is the LDS PA100E signal amplifier that was used to drive the LDS V400 electromagnetic shaker. The control of the shaker input and data acquisition was carried out using a LabView system running on a laptop PC. Using this experimental test system, several configurations of the inerter system were considered.

3.1. Experimental configurations

Four rig configurations were used during the experimental testing. All configurations were tested across the 10–60Hz frequency range to fully characterise the response. The configurations were:

- Configuration 1 was the shaker with an accelerometer attached directly to its armature and to the cantilever plate above the shaker. This configuration was used to characterise any interaction of the shaker with its support structures.

- Configuration 2 included a mass attached to the shaker via a stinger and suspension system in the no-springs, no-inerter layout shown schematically in Figure 6 (a). This configuration allowed the interaction of the mass and stinger to be characterised and the stinger length selection to be verified.
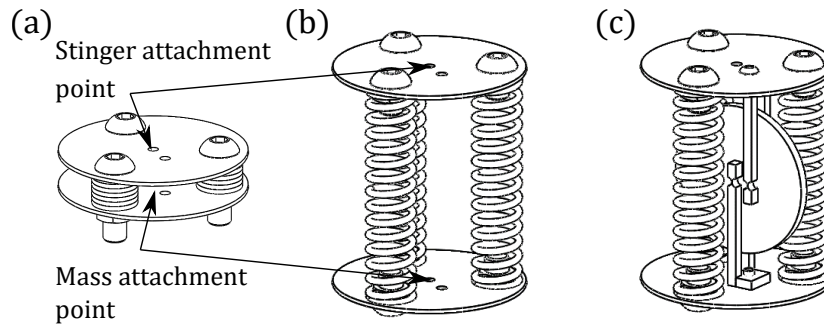
11

Figure 6: Suspension system layouts used during testing. (a) Configuration 2 layout. (b) Configuration 3 layout with springs fitted. (c) Configuration 4 layout with springs and living-hinge inerter fitted. Each layout had a 0.2 kg mass fitted beneath the location marked *Mass attachment point*. See also the photographs in Figure 7.

Accelerometers were also fitted on the mass, directly to the shaker armature, and to the cantilever plate, allowing any effects caused by stinger and mass interaction to be identified.

- Configuration 3 included the springs and mass, as shown schematically in Figure 6 (b), and the final working version in Figure 7 (a). This arrangement allowed the response of the mass-spring system across the frequency range to be tested without the inerter. To record the experimental data, accelerometers were placed on the suspension top plate and bottom plate (as can be seen in Figure 7), as these corresponded to the two terminals of the springs and allowed displacement transmissibility to be calculated. This will be called the *uncontrolled* system.

- Configuration 4 was the mass-spring system with the living-hinge inerter fitted, as shown in Figure 6 (c), and the final working version in Figure 7 (b). This will be called the *inerter* system.

The key configurations used to give the results in this paper are Configurations 3 (uncontrolled) and 4 (inerter), which are shown respectively in Figure 7 (a) and (b). The other parameter values of the system measured or calculated as part of the experimental procedure are given in Table 1. Note that the apparently high inertance to mass ratio is due to the relatively lightweight materials used in this experiment. We now described the experimental results obtained from these configurations.
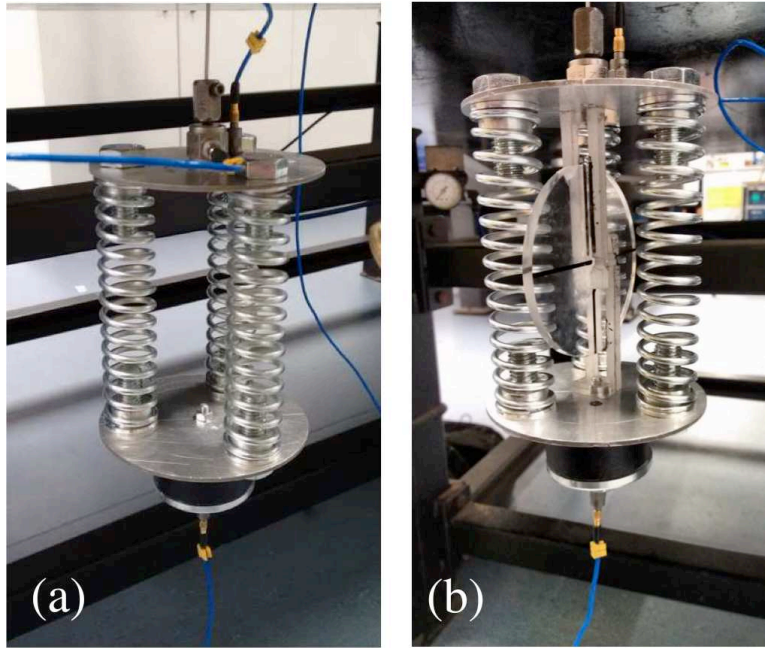
Figure 7: Photograph of the inerter test system, showing (a) the spring mass system without the inerter, and (b) the spring mass system with the living-hinge inerter fixed in position.

Property	Value	Units	Comment
Mass of the oscillator (M)	0.459	kg	Measured
Flywheel radius (r_f)	0.04	m	Design
Flywheel depth (d_f)	0.005	m	Design
Lever arm length (ℓ_a)	0.01	m	Design
Flywheel mass (m_f)	0.0268	kg	Measured
Flywheel inertia (I)	2.14x10^{-5}	kgm^2	$(r_f^2 m_f)/2$
Device inertance (b)	0.214	kg	Eqn. (3)
Inertance to mass ratio (μ)	0.467	-	$\mu = b/M$

Table 1: System parameters
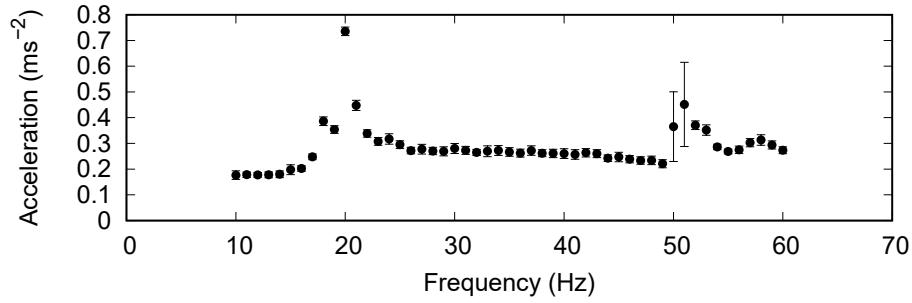
(a)
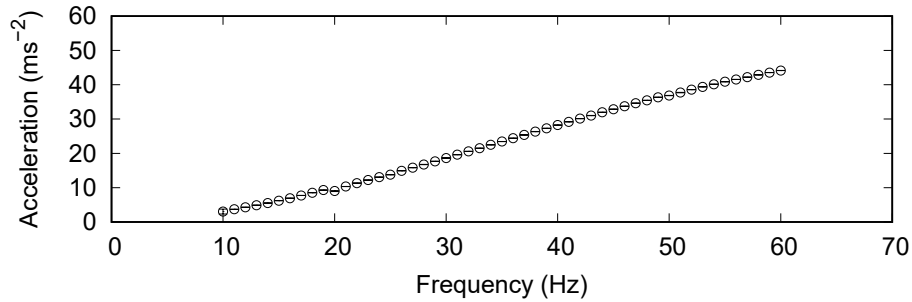
(b)

Figure 8: Results from Configuration 1 showing the measured acceleration values from (a) the cantilever support measured at the tip, and (b) the shaker armature. The mean acceleration values are shown with an error of ± one standard deviation. As can be seen from (a) the only place where the error bars are visible is close to 50Hz indicating that only in this region was there any significant variability in the data.

4. Experimental Results

4.1. Preliminary testing

The initial testing was carried out in Configurations 1 and 2 to assess the dynamic behaviour of the support structure and shaker. The test procedure was to use a stepped sine excitation input [39, 40] across the frequency range at 1Hz intervals. For each frequency value in the range, the steady state acceleration signal was recorded and the mean and standard deviation of the results calculated. An example is shown in Figure 8, where a representative sample of the results from Configuration 1 are shown. It can be seen From Figure 8 (a) that the cantilever support plate (when used in Configuration 1) has two resonances in the $10-60$Hz frequency range. The resonances peaks appeared at 20Hz and 51Hz, although in

14

both cases the amplitudes of acceleration are below 1m/s^2. Given these relatively low amplitudes (an order of magnitude lower than the mass-spring system) it was decided not to modify the cantilever plate or support structure. Another factor in this decision was that any additional stiffening of the plate would have moved the 20Hz resonance closer to that of the resonance of the mass-spring oscillator system, which would have been undesirable. The results shown in Figure 8 (b) show that there is an approximately linear increase in acceleration amplitude recorded at the shaker armature.

Results from preliminary testing of Configuration 2 are shown in Figure 9. Note that now, there are four accelerometer readings. As before, the accelerations of the cantilever support plate are recorded. These are still at a relatively low amplitude, but note that the first resonance peak has shifted slightly down in frequency to approximately 18Hz. This is caused by the extra mass now suspended from the cantilever plate, and the second resonance also shifts down from 51Hz to 48Hz. It can be observed that at the 18Hz resonance frequency, there appears to be some interaction with the other signals.

The accelerometer readings from the top plate and bottom plate represent the terminals of the springs, and for Configuration 1 they should be the same, because the terminals are rigidly fixed together. This holds true for the frequency range below 44Hz, but we note that above 44Hz there is some small variation between the signals. This difference, appears most significant close to 50Hz, and a possible influence on this is the cantilever plate resonance at 48Hz. Although the amplitudes of the cantilever plate itself at this frequency are very small, there appears to be an interaction. Specifically by observing the top-plate signal, it can be seen that there is a clear jump in acceleration value at 48Hz. A small jump in acceleration amplitude can also be observed in the bottom plate signal at the same point.

The last signal recorded is the acceleration of the shaker armature. Ideally, this should be the same as the top plate signal, as they are connected by the stinger. A selection of stinger lengths were tested, and it was found that a 30 mm stinger was the most preferable length, in terms of minimising unwanted stinger vibrations, when compared to other choices. Even so, a small amount of axial stinger motion is still present in the higher frequency range, and can be observed in Figure 9 above 32Hz, as a small divergence of the top-plate and shaker armature signals.

The preliminary phase of testing was concluded, having enabled the possible influence of the supporting structure on the main results to be characterised. The main observations were that the cantilever plate resonance had shifted to 18Hz, and appeared to cause some interaction with the other recorded signals. The cantilever plate resonance at 51Hz had shifted to 48Hz, and also appeared to cause
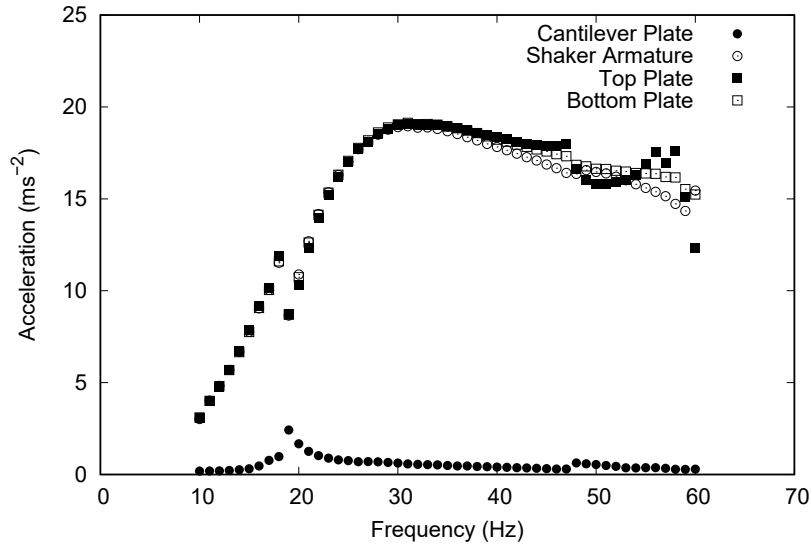
Figure 9: Rig configuration 2 measured acceleration. Averaged acceleration values are shown. Error bars are not included as they are too small to show.

some interaction with the other recorded signals. Lastly some axial motion in the stinger was observed in the higher frequency range.

4.2. Results from the mass-spring-inerter system

Having commissioned the test rig, and carried out the preliminary testing, the next phase of experimental work was to test the mass-spring-inerter system. This was carried out in two stages. First the uncontrolled mass-spring system (Configuration 3) was tested. Then finally, the full mass-spring-inerter system (Configuration 4) was tested.

Representative data sets from each of these two test configurations are shown in Figures 10 and 11 respectively. The results shown in these two figures give the mean steady-state acceleration measurements recorded at each frequency interval during the stepped sine testing. This data was acquired in the same way as for Configurations 1 and 2, with the exception that once the data was acquired at a 1Hz resolution, areas of particular interest were re-sampled at a resolution of 0.25Hz. This provided much greater detail particularly around the resonance and anti-resonance features.

It can be observed from both plots that the motion of the cantilever support is still present, but at a relatively low amplitude. The cantilever plate resonance at 18Hz appears to have an influence on other signals, but the 48Hz influence
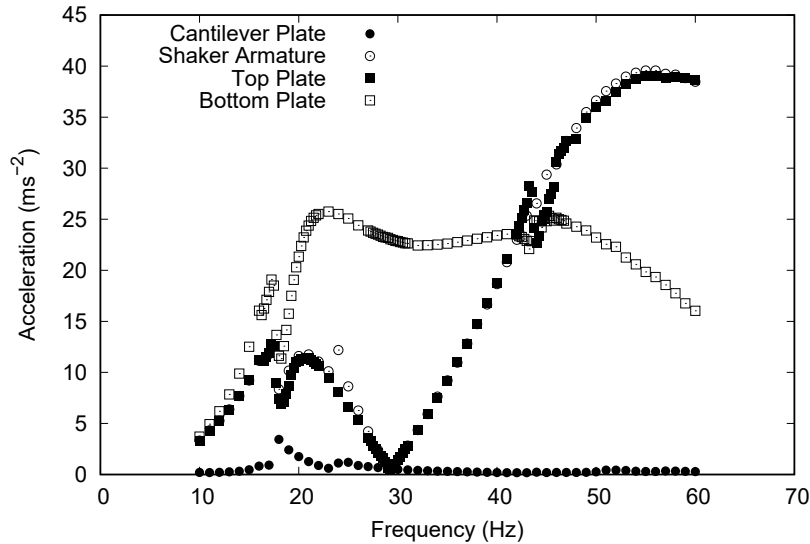
16

Figure 10: Rig Configuration 3 for the uncontrolled system showing the measured accelerations. Error bars are not included as they are too small to show.

appears minimal. The stinger motion is minimal in the results shown in Figures 10, although there is some motion in Figure 11, particularly between 50Hz and 60Hz.

The influence of the inerter was something that could not be captured in the preliminary testing. It was found from high-speed footage recorded during initial test runs for Configuration 4, that the inerter was in a slightly off-centre position, which caused unwanted sway motions, particularly at the resonant and anti-resonant frequencies. The rig was then modified to relocate the inerter more centrally, which had the desired effect of reducing unwanted sway motions.

4.3. Transmissibility of the mass-spring-inerter system

The transmissibility of both uncontrolled (Configuration 3) and inerter (Configuration 4) was found by dividing the acceleration amplitude values of the mass, $\ddot{x}$, (bottom plate in the experiment) by the acceleration amplitude values of the input, $\ddot{y}$ (top plate in the experiment) and is shown in Figure 12. This transmissibility plot shows much more clearly the effect of adding the inerter to the system. Note that the experimentally recorded data is shown as open circles for the uncontrolled mass-spring system and solid dots of the system with the inerter added. The uncontrolled system has just a single resonance at 29.25Hz. When the inerter is
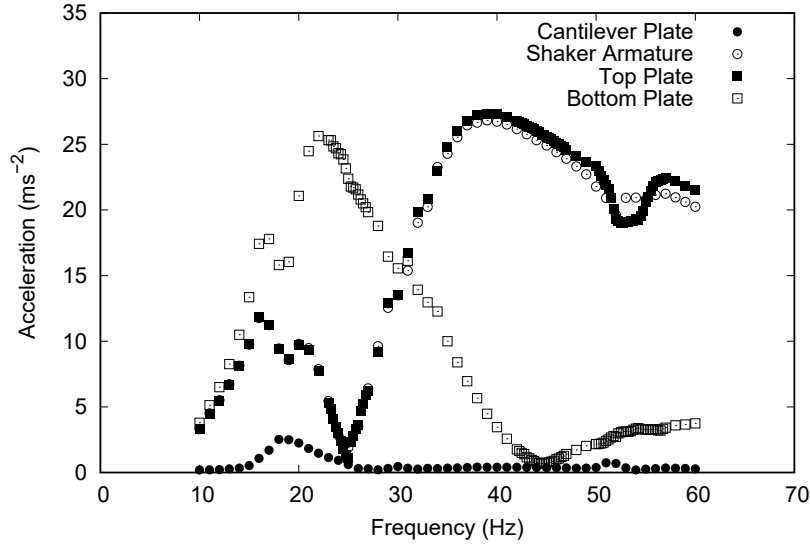
17

Figure 11: Rig Configuration 4 for the inerter system showing the measured accelerations. Error bars are not included as they are too small to show.

added, this resonance reduces to approximately 25Hz, and a large anti-resonance is created at 44Hz.

The isolation effect in terms of amplitude is very significant. In this case the reduction of amplitude between the highest point on the uncontrolled resonance peak to the lowest point in the anti-resonance is at least three orders of magnitude. Although we note that the anti-resonance is at a different frequency to the uncontrolled resonance, it is possible by adjusting the inertance, to align these frequencies, as shown in Figure 2.

Note that there are some small disturbances to the experimental transmissibility recordings, notably in the region of 44Hz and 53.5Hz which were determined to be due to resonant behaviour of the cantilever support as discussed previously.

The solid lines shown in Figure 12 are from the theoretical model presented in Section 2.1. Using Equations (9) and (10), we can compare the transmissibility function from the experimental acceleration signals to the model. In order to make this comparison the following measured values were used; free mass $m = 0.459$ kg, uncontrolled resonance $\omega_n = 29.25$Hz, inerter resonance $\omega_r = 25$Hz, and anti-resonance $\omega_a = 44.5$Hz. Spring stiffness was not considered a measured variable as the value of 15.87 kN/m quoted in Table 1 was based only on the manufacturers specifications. Using the natural frequency values, the stiffness of the uncon-
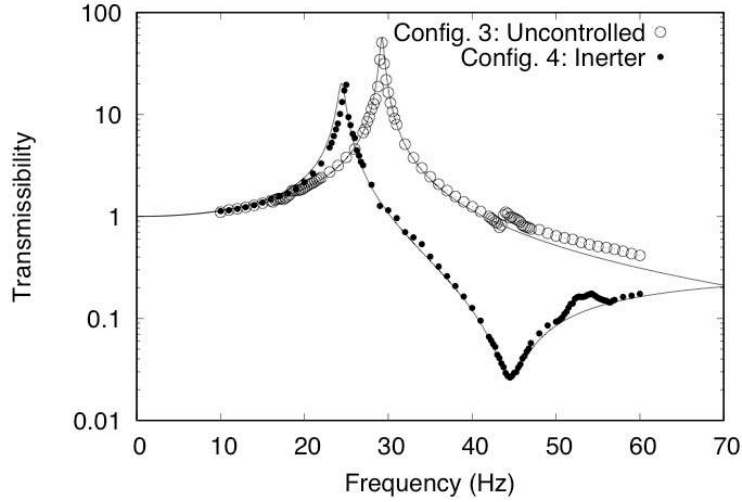
18

Figure 12: Comparison of the transmissibility of the system. The experimental data is shown as uncontrolled (Configuration 3) with circles, and inerter (Configuration 4) with black dots. The solid lines show the mathematical models for each case.

trolled system was calculated to be $k = 15.5$ kN/m, which is acceptably close to the manufacture's value. Equation (8) was rearranged to give a single equation for inertance in terms of mass and the resonant and anti-resonant frequencies. Using the measured mass and frequency values above, the inertance of the inerter controlled system was calculated to be $b = 0.212$ kg. Estimating the damping coefficient c was initially carried out using the half-power bandwidth method. The values obtained were then adjusted manually to give a better fit to the experimental data leading to final values of $c = 1.5$ kg/s (damping ratio $\zeta = 0.009$) for the uncontrolled system and $c = 3.5$ kg/s (damping ratio $\zeta = 0.021$) for inerter system.

Using these parameter values, the theoretical models matched the experimental data closely and resulted in a mean error of 2.81 % for the uncontrolled system (Configuration 3) and a mean error of 6.56 % for the inerter system (Configuration 4).

Another important factor is the estimated increase in system damping from $c = 1.5$ kg/s for uncontrolled to $c = 3.5$ kg/s for the inerter system. As the only change between the two configurations was the inclusion of the inerter, this increase in damping of 2 kg/s must represent the additional damping from the inerter. In non-dimensional terms this corresponds to an increase in damping ratio, ζ, for the uncontrolled system of 1.2%. The primary source of this damping is the

19

energy required to deform the living-hinges while the inerter operates, and to the authors knowledge there are currently no mathematical models via which this type of damping can be quantified. Similarly, we conclude that the living-hinges must also cause a small increase in stiffness, which was measured to be approximately a 1.1 kN/m increase, based on using Equation (8) for the inerter system data. In summary, these results show that the living-hinge inerter had an inertance of approximately $b = 0.212$ kg, an equivalent viscous damping of $c = 2$ kg/s, and an equivalent linear stiffness of $k = 1.1$ kN/m over the frequency range $20 - 50$Hz. This was with a maximum relative terminal displacement of 1 mm (estimated from the relative acceleration data using the harmonic motion assumption) and a maximum relative terminal acceleration of 25 ms^{-2}.

5. Conclusions

In this paper a novel type of frictionless mechanical inerter device has been presented, where instead of gears, motion of the flywheel is achieved using *living-hinges*. As a starting point, the design was considered as a pivoted flywheel inerter inspired by the DAVI system, first developed in the 1960s. It was noted that a pivoted flywheel inerter had the advantage of producing balanced forces, and could also be modelled using a simple model, that was presented in detail in Section 2.1.

Having established an overall mathematical model, the detailed design of the living-hinges was carried out. This involved calculating the geometry of the hinges to enable the required displacements of the flywheel to occur during operation. Following this, the experimental procedure was described, including details of the test apparatus, and four different test configurations used.

The experimental results were presented in Section 4. Preliminary testing was used to identify the influence of the supporting structures on the inerter test rig. Then the uncontrolled mass-spring system, and the inerter system were tested. These results were converted into transmissibility values, that could be compared to the mathematical model from Section 2.1.

The results showed that the living-hinge inerter provided an isolation effect of at least three orders of magnitude in terms of the maximum amplitude reduction. The living-hinges did introduce additional damping, and this was found to corresponds to an increase in damping ratio, ζ, for the uncontrolled system of 1.2%.

Finally, we refer back to the conditions defined by Smith in 2002 [1], and stated in Section 2, which an inerter must meet in order to be of practical use. The living-hinge inerter developed in this paper satisfies all of these criteria. In

addition, it operates without mechanical friction, or fluid flow, and so represents a new paradigm in experimental inerter technology.

6. Acknowledgements

References

[1] M. C. Smith, Synthesis of mechanical networks: the inerter, IEEE Transactions on Automatic Control 47 (10) (2002) 1648–1662.

[2] W. G. Flannelly, Dynamic antiresonant vibration isolator, US Patent 3,322,379 (May 30 1967).

[3] R. A. Desjardins, W. Hooper, Antiresonant rotor isolation for vibration reduction, Journal of the American Helicopter Society 25 (3) (1980) 46–55.

[4] N. Liu, C. Li, C. Yin, X. Dong, H. Hua, Application of a dynamic antiresonant vibration isolator to minimize the vibration transmission in underwater vehicles, Journal of Vibration and Control (2017) 1077546317711538.

[5] C. Yilmaz, N. Kikuchi, Analysis and design of passive band-stop filter-type vibration isolators for low-frequency applications, Journal of Sound and Vibration 291 (3-5) (2006) 1004–1028.

[6] P. G. Dylejko, I. R. MacGillivray, On the concept of a transmission absorber to suppress internal resonance, Journal of Sound and Vibration 333 (10) (2014) 2719–2734.

[7] W. C. Flower, Understanding hydraulic mounts for improved vehicle noise, vibration and ride qualities, SAE Technical Paper 1 (1985) 850975.

[8] R. Singh, Dynamic design of automotive systems: Engine mounts and structural joints, Sadhana 25 (3) (2000) 319–330.

[9] M. F. Golnaraghi, G. Nakhaie Jazar, Development and analysis of a simplified nonlinear model of a hydraulic engine mount, Journal of vibration and control 7 (4) (2001) 495–526.

[10] P. Soltani, C. Pinna, D. J. Wagg, R. Whear, Ageing simulation of a hydraulic engine mount – a data informed finite element approach, accepted for publication in: Proc. IMechE, Part D: Journal of Automobile Engineering.

[11] K. Ikago, Y. Sugimura, K. Saito, N. Inoue, Modal response characteristics of a multiple-degree-of-freedom structure incorporated with tuned viscous mass dampers, Journal of Asian Architecture and Building Engineering 11 (2) (2012) 375–382.

[12] M. Z. Chen, C. Papageorgiou, F. Scheibe, F.-C. Wang, M. C. Smith, The missing mechanical circuit element, IEEE Circuits and Systems Magazine 9 (1) (2009) 10–26.

[13] S. Evangelou, D. J. Limebeer, R. S. Sharp, M. C. Smith, Steering compensation for high-performance motorcycles, in: Decision and Control, 2004. CDC. 43rd IEEE Conference on, Vol. 1, IEEE, 2004, pp. 749–754.

[14] C. Papageorgiou, N. E. Houghton, M. C. Smith, Experimental testing and analysis of inerter devices, Journal of dynamic systems, measurement, and control 131 (1) (2009) 011001.

[15] A. Kuznetsov, M. Mammadov, I. Sultan, E. Hajilarov, Optimization of improved suspension system with inerter device of the quarter-car model in vibration analysis, Archive of Applied Mechanics 81 (10) (2011) 1427–1437.

[16] F.-C. Wang, H.-A. Chan, Vehicle suspensions with a mechatronic network strut, Vehicle System Dynamics 49 (5) (2011) 811–830.

[17] M. C. Smith, F.-C. Wang, Performance benefits in passive vehicle suspensions employing inerters, Vehicle System Dynamics 42 (4) (2004) 235–257.

[18] R. Wang, X. Meng, D. Shi, X. Zhang, Y. Chen, L. Chen, Design and test of vehicle suspension system with inerters, Proceedings of the Institution of Mechanical Engineers, Part C: Journal of Mechanical Engineering Science 228 (15) (2014) 2684–2689.

[19] F.-C. Wang, M.-K. Liao, B.-H. Liao, W.-J. Su, H.-A. Chan, The performance improvements of train suspension systems with mechanical networks employing inerters, Vehicle System Dynamics 47 (7) (2009) 805–830.

[20] F.-C. Wang, M.-K. Liao, The lateral stability of train suspension systems employing inerters, Vehicle System Dynamics 48 (5) (2010) 619–643.

[21] F.-C. Wang, M.-F. Hong, C.-W. Chen, Building suspensions with inerters, Proceedings of the Institution of Mechanical Engineers, Part C: Journal of Mechanical Engineering Science 224 (8) (2010) 1605–1616.

[22] I. Takewaki, S. Murakami, S. Yoshitomi, M. Tsuji, Fundamental mechanism of earthquake response reduction in building structures with inertial dampers, Structural Control and Health Monitoring 19 (6) (2012) 590–608.

[23] I. F. Lazar, S. A. Neild, D. J. Wagg, Using an inerter-based device for structural vibration suppression, Eathquake Engineering & Structural Dynamics 43 (8) (2014) 1129–1147, dOI: 10.1002/eqe.2390.

[24] I. F. Lazar, S. A. Neild, D. J. Wagg, Vibration suppression of cables using tuned inerter dampers, Engineering Structures 122 (2016) 62–71.

[25] A. Giaralis, A. Taflanidis, Optimal tuned mass-damper-inerter (tmdi) design for seismically excited mdof structures with model uncertainties based on reliability criteria, Structural Control and Health Monitoring 25 (2) (2018) e2082.

[26] D. De Domenico, G. Ricciardi, An enhanced base isolation system equipped with optimal tuned mass damper inerter (tmdi), Earthquake Engineering & Structural Dynamics 47 (5) (2018) 1169–1192.

[27] Y. Hu, J. Wang, M. Chen, Z. Li, Y. Sun, Load mitigation for a barge-type floating offshore wind turbine via inerter-based passive structural control, Engineering Structures 177 (2018) 198–209.

[28] M. C. Smith, Force-controlling mechanical device, US Patent 7,316,303 (Jan. 8 2008).

[29] Z. Ge, W. Wang, Modeling, testing, and characteristic analysis of a planetary flywheel inerter, Shock and Vibration 2018. Article ID 2631539: 1-12.

[30] S. Swift, M. Smith, A. Glover, C. Papageorgiou, B. Gartner, N. Houghton, Design and modelling of a fluid inerter, International Journal of Control 86 (11) (2013) 2035–2051.

[31] F.-C. Wang, M.-F. Hong, T.-C. Lin, Designing and testing a hydraulic inerter, Proceedings of the Institution of Mechanical Engineers, Part C: Journal of Mechanical Engineering Science 225 (1) (2011) 66–72.

[32] N. Smith, D. J. Wagg, A fluid inerter with variable inertance properties, in: Proceedings of the 6th European Conference on Structural Control, 2016, pp. 1–8, https://doi.org/10.15131/shef.data.4206096.v1.

[33] M. Saitoh, On the performance of gyro-mass devices for displacement mitigation in base isolation systems, Structural Control and Health Monitoring 19 (2) (2012) 246–259.

[34] Y. Hu, M. Z. Chen, Z. Shu, L. Huang, Analysis and optimisation for inerter-based isolators via fixed-point theory and algebraic solution, Journal of Sound and Vibration 346 (2015) 17–36.

[35] M. Z. Q. Chen, Y. Hu, L. Huang, G. Chen, Influence of inerter on natural frequencies of vibration systems, Journal of Sound and Vibration 333 (7) (2014) 1874–1887.

[36] S. T. Smith, Flexures, Boca Raton : CRC Press LLC, 2000, pp. 177-191.

[37] P. A. Tres, Living Hinges: Designing plastic parts for assembly, Munich: Hanser Publishers, 2017.

[38] K. L. Edwards, A designers' guide to engineering polymer technology., Materials and Design, 19 (1998,) 57–67.

[39] F. Lembregts, P. Sas, H. Van Der Auweraer, J. Leuridan, Integrated stepped-sine system for modal analysis, Mechanical Systems and Signal Processing 1 (4) (1987) 415–424.

[40] K. G. McConnell, P. S. Varoto, Vibration Testing: Theory and Practice, Hoboken : John Wiley & Sons, 2008.

Appendix A. Living-hinge inerter model dimensions

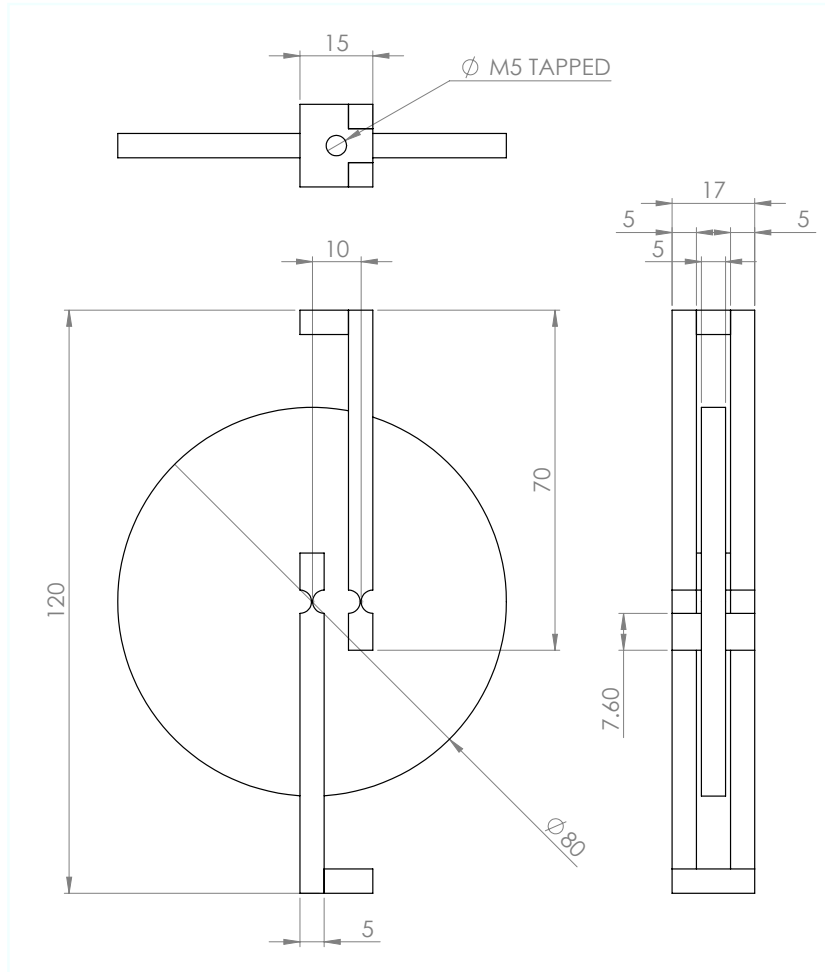A dimensioned drawing used for the manufacture of the living hinge inerter is shown in Figure A.13.

Figure A.13: Dimensioned third angle projection of the inerter model used in testing.